

Technical Report No. 32-743

**Low Subsonic Dynamic-Stability Investigation of Several
Planetary-Entry Configurations in a Vertical Wind Tunnel
(Part I)**

Jack E. Marte

Robert W. Weaver

N65-24985

(ACCESSION NUMBER)

18

(PAGES)

CR 63117

(NASA CR OR TMX OR AD NUMBER)

(THRU)

1

(CODE)

01

(CATEGORY)

GPO PRICE \$ _____

OTS PRICE(S) \$ _____

Hard copy (HC) 1.00

Microfiche (MF) .50

jpl

JET PROPULSION LABORATORY
CALIFORNIA INSTITUTE OF TECHNOLOGY
PASADENA, CALIFORNIA

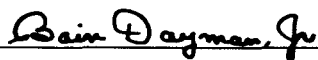
May 1, 1965

Technical Report No. 32-743

*Low Subsonic Dynamic-Stability Investigation of Several
Planetary-Entry Configurations in a Vertical Wind Tunnel
(Part I)*

Jack E. Marte

Robert W. Weaver



Bain Dayman, Jr., Manager
Aerodynamic Facilities Section

JET PROPULSION LABORATORY
CALIFORNIA INSTITUTE OF TECHNOLOGY
PASADENA, CALIFORNIA

May 1, 1965

Copyright© 1965
Jet Propulsion Laboratory
California Institute of Technology

Prepared Under Contract No. NAS 7-100
National Aeronautics & Space Administration

FIGURES (Cont'd)

7. Wind-tunnel model, L-shape	4
8. Wind-tunnel model, M-shape	4
9. Wind-tunnel model, N-shape	4
10. Wind-tunnel model, L-shape forebody with 0.70-d hemispherical afterbody	4
11. Sketches of model test configurations	5
12. Axis system	7

CONTENTS

I. Introduction	1
II. Facilities, Models, and Testing	1
III. Data Reduction	6
IV. Results	8
V. Discussion	9
VI. Summary	10
Nomenclature	11
References	12

TABLES

1. Characteristics of the Langley 20-ft free-spinning tunnel	2
2. Center-of-gravity (c.g.) locations and moments of inertia of the various models tested	6
3. Pitching-moment curve slope (per rad), C_{m_α}	7
4. Side-force curve slope (per rad), C_{z_α}	7
5. Dynamic drag coefficient, C_D	8
6. Other model parameters	9
7. Dynamic-damping parameter (per rad), $\bar{C}_{m_{\dot{\alpha}}}$	9

FIGURES

1. Model drawing, P-shape	2
2. Model drawing, L-shape	2
3. Model drawing, M-shape	2
4. Model drawing, N-shape	3
5. Model drawing of three hemispherical afterbodies	3
6. Wind-tunnel model, P-shape	4

FOREWORD

Part II of this Report, containing classified test information about the *Apollo* configuration (*P*-shape) and relating to the investigation in this present Report, will be published as JPL Technical Memorandum No. 33-215 (Part II), dated May 1, 1965.

ABSTRACT

24985

An experimental investigation of the dynamic-damping parameter, \bar{C}_{mq} , for a series of possible Mars-entry configurations was performed in the Langley 20-ft free-spinning tunnel at low subsonic velocities. Several of the tested configurations exhibited satisfactory dynamic characteristics including the ability to recover from angular deflections up to 80 deg. The effect of afterbody shape and maximum angle of oscillation on the dynamic stability of certain configurations was ascertained. Drag and pitching-moment data were also obtained.



I. INTRODUCTION

An investigation was conducted to provide low subsonic (0 to 90 ft/sec) dynamic-stability data for a further evaluation of a ballistic deceleration vehicle entering the Mars atmosphere. These data are required to determine if the configuration in question would remain properly oriented during the subsonic phase of the trajectory immediately prior to impact. If proper orientation could be maintained, the amount of energy-absorbing structure could be minimized.

The facility used for this investigation was the Langley 20-ft free-spinning tunnel located at Langley Research

Center, Hampton, Virginia. The tunnel test section has a vertically-rising column of air traveling at speeds up to 90 ft/sec. This velocity is not as high as expected terminal velocities on Mars but affords data in the Mach-zero region for an unrestrained model at atmospheric (Earth) supply pressure. The data consist of motion pictures of the model during flight. Tests were conducted during August, 1964.

The data from one of the configurations tested are classified, and a separate classified Report, JPL TM 33-215 (Part II) which includes these data, is being published concurrently with this present Report.

II. FACILITIES, MODELS, AND TESTING PROCEDURES

The Langley 20-ft free-spinning tunnel was chosen for these tests because the vertical orientation of the flow permitted free flight under equilibrium conditions over relatively long periods of time.

The data obtained were in the form of motion pictures¹ taken at a film speed of 64 frames/sec. As the camera

photographed the motion, it also photographed readings of a timing device and of a pitot-static tube; thus, records of time and velocity were recorded simultaneously with the model motion. Table 1 and Ref. 1 give some further details about the tunnel.

The models were constructed of ten layers of fiberglass and resin.² The final nominal wall thickness was 0.05 in.

¹The unedited film is on file at the Jet Propulsion Laboratory, Aerodynamic Facilities Section, and at the Langley Research Center, 20-ft Free-Spinning Tunnel.

²These models were built on a contract basis by Tolo Inc., Fullerton, Calif.

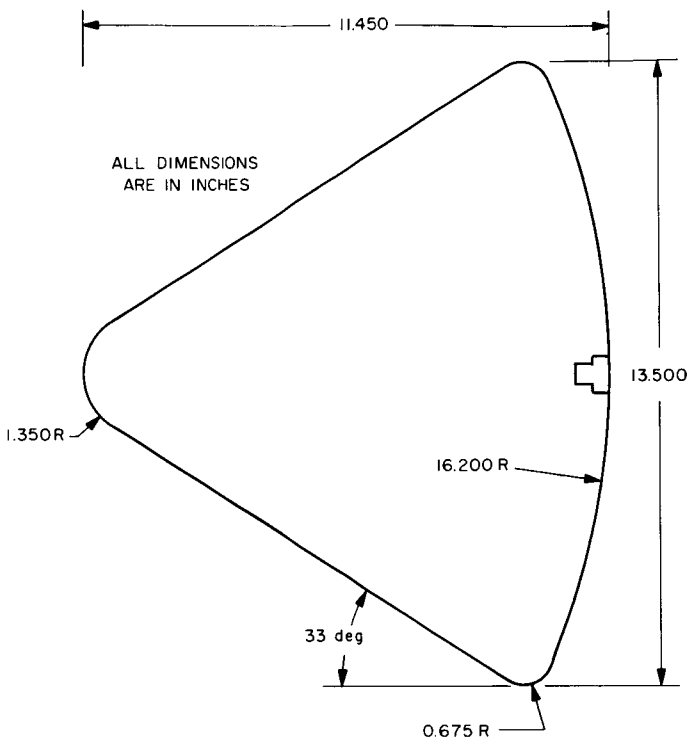


Fig. 1. Model drawing, P-shape

Table 1. Characteristics of the Langley 20-ft free-spinning tunnel	
Speed range, ft/sec	0 to 97
Dynamic pressure, psf	0 to 11
Reynolds No./ft:	
Idling	84×10^3
Maximum	62×10^4
Test section:	
Position	vertical
Number of sides	12
Distance across flats, ft	20
Length (vertical), ft	25½
Type throat	closed
Return passage	annular
Air flow:	
Smooth, with increasing velocity gradient of 6% from center to three-fourths of tunnel radius; stable vertical-velocity gradient (slight divergence of walls)	
Max acceleration of airstream, ft/sec ²	15
Max deceleration of airstream, ft/sec ²	25
Method of smoothing:	
Two sets of turning vanes downstream of end of exit cone; honeycomb and screens in entrance cone	
Turbulence factor	2.0

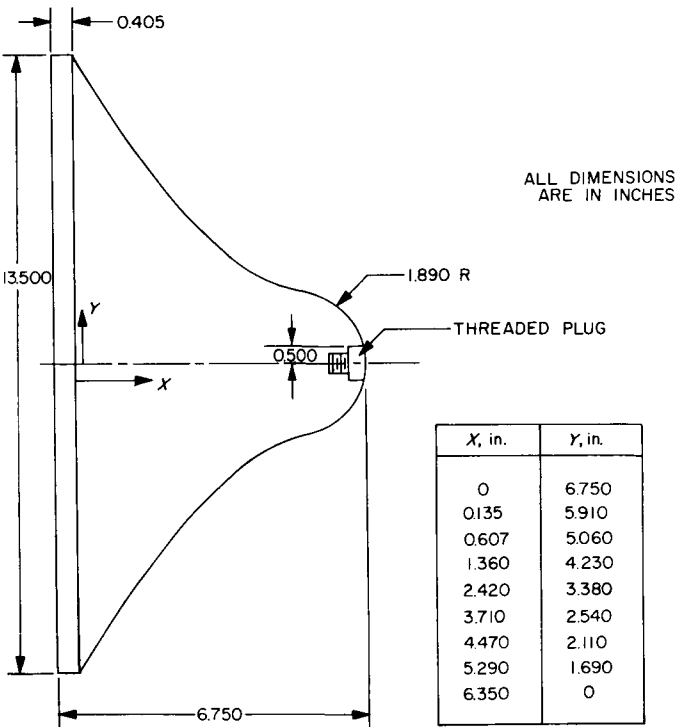


Fig. 2. Model drawing, L-shape

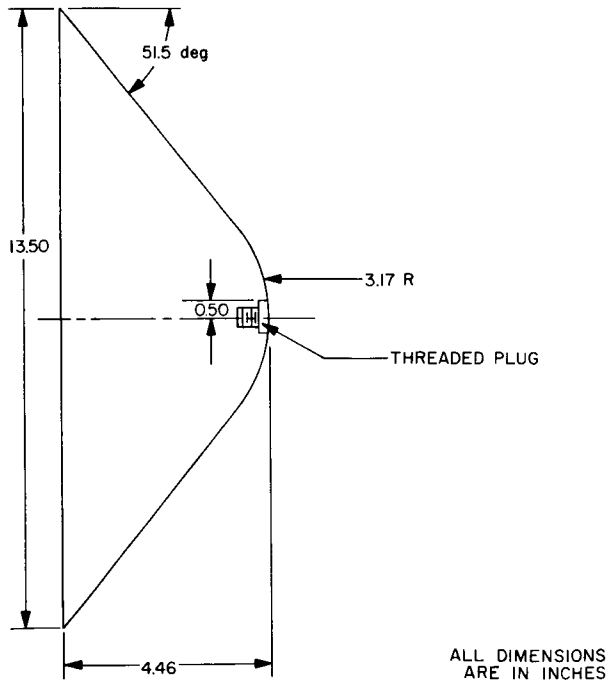


Fig. 3. Model drawing, M-shape

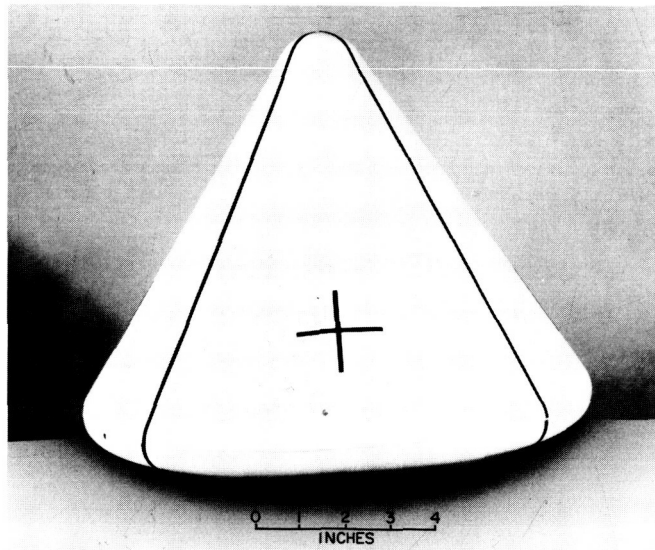


Fig. 6. Wind-tunnel model, P-shape

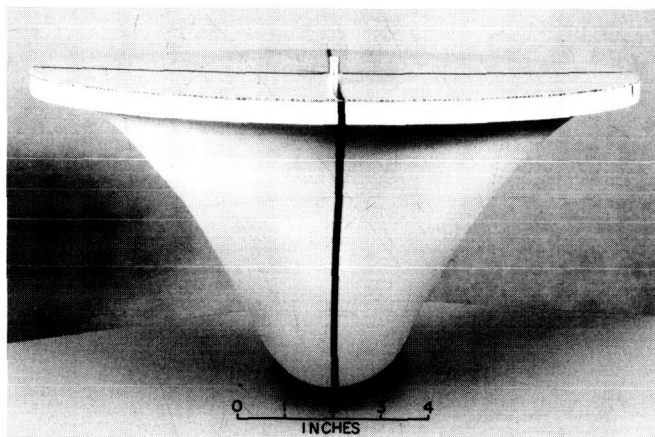


Fig. 7. Wind-tunnel model, L-shape

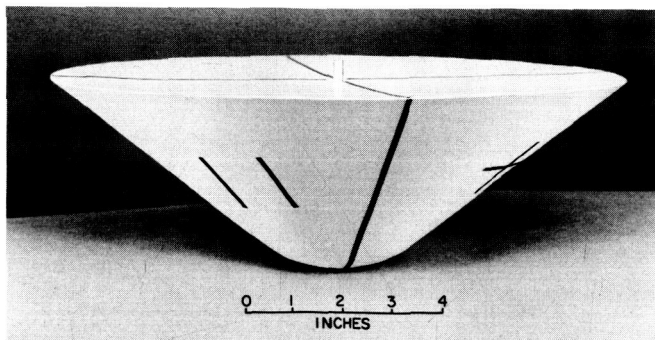


Fig. 8. Wind-tunnel model, M-shape

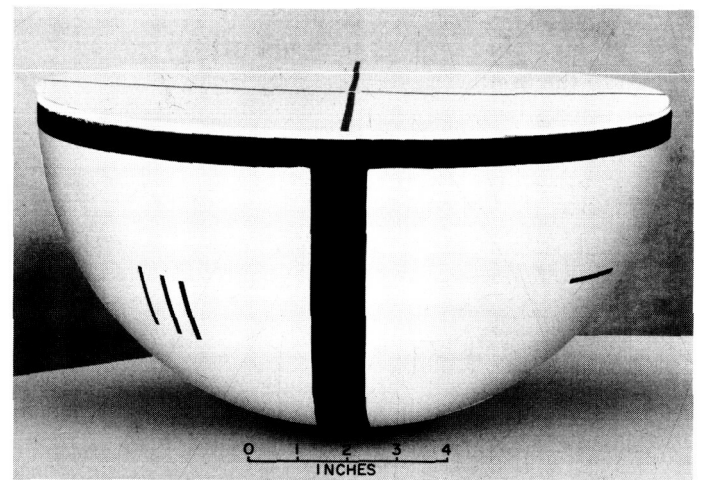


Fig. 9. Wind-tunnel model, N-shape

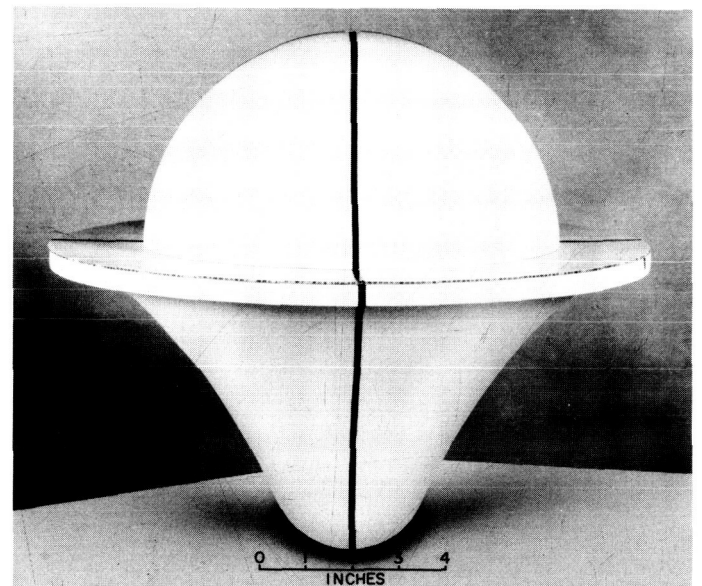


Fig. 10. Wind-tunnel model, L-shape forebody with 0.70-d hemispherical afterbody

released, and the time for five complete cycles was recorded. This time, combined with known constants and model parameters, was used to determine the moments of inertia about each of the three axes.

Prior to the test a table of moments of inertia for the full-scale configurations was supplied. The lead weights were located in the models in such a manner so as to insure that I_Y/I_X values were in approximate proportion to the full-scale configurations.

Four nose shapes were constructed; they were the *P*-shape (see Fig. 1), the *L*-shape (see Fig. 2), the *M*-shape (see Fig. 3) and the *N*-shape (see Fig. 4). The five afterbody shapes constructed were the *P*-shape afterbody, a flat-plate afterbody, and hemispherical afterbodies of three diameters (see Fig. 5). During the test the *M*-shape nose and the *L*-shape nose were also used as afterbodies. The models for which quantitative data were obtained are shown in Fig. 6 through 10. Figure 11 contains sketches of all configurations tested including those for which only qualitative data were obtained.

An internally-threaded aluminum plug was built into each nose. This plug served (1) as a mounting point by which the model was attached to devices used for measuring moments of inertia and c.g. locations, and also (2) as an attachment point for the center rod used to secure the afterbodies to the noses. The afterbodies were secured to the rod by a set screw. When the models were assembled, the seam between the nose and the afterbody was sealed with tape. The models were also marked with tape to facilitate the identification of the model orientation.

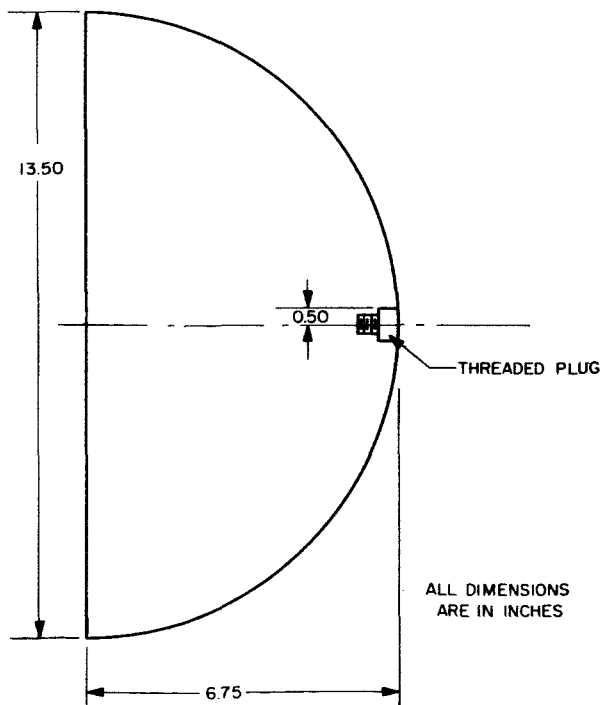


Fig. 4. Model drawing, *N*-shape

The centers of gravity (c.g.'s) of the models were located by using a beam balance. The models were attached to a beam-balance arm at a known distance from the fulcrum. Known weights were then hung on the other arm of the balance. A simple computation of the moments about the fulcrum resulted in the coordinates of the c.g. by using the plug in the nose as the origin. Lead weights were used to place the c.g. at the desired point.

Prior to the test it was determined that the c.g.'s should be 0.14 to 0.18 *d* (max *d* was always used, viz., 13.5 in.) from the nose of the model. However, some of the afterbodies were of such size and weight that the desired c.g. location could not be obtained. The limitation of tunnel-flow velocity and the drag coefficient imposed an upper limit on over-all weight. This problem was further complicated by the requirement to maintain moments of inertia that were realistic. Moments of inertia were maximized as far as possible within the constraints of model size, construction, c.g. location, and total-weight limitations. Table 2 gives all c.g. locations and moments of inertia.

The moments of inertia were found by using a spring-actuated rotating mechanism. The model was mounted in the desired orientation on the mechanism, a trigger was

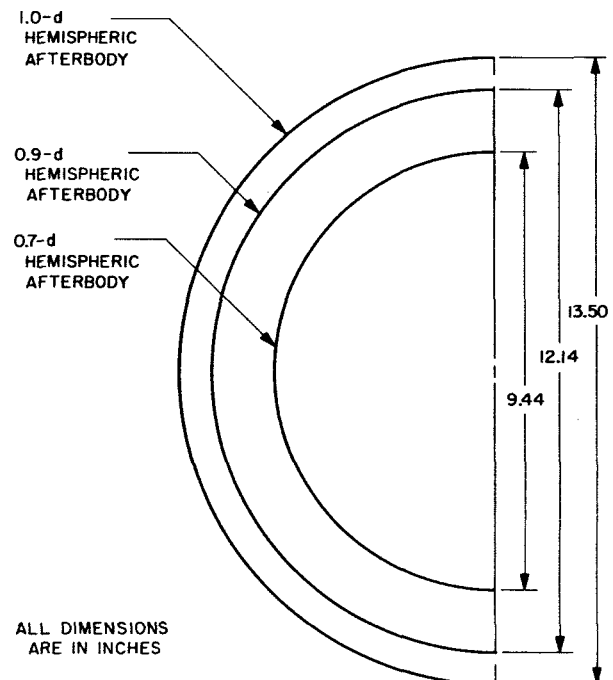


Fig. 5. Model drawing of three hemispherical afterbodies

When the weights had been placed in the proper locations to give the desired moments of inertia and c.g. location, the models were assembled for testing. The actual testing of the models required a camera operator and a model launcher in addition to a tunnel operator. The tunnel test-section window was opened, and the model was held in the desired orientation in the tunnel while

the tunnel operator adjusted the tunnel air speed. This speed was found by momentarily releasing the model to see if it would rise or fall. When the model remained relatively stable, the person launching the model would signal the tunnel operator. The tunnel operator would turn on a bank of photo floodlights, which was a signal to the camera operator to begin taking pictures. Also, the model

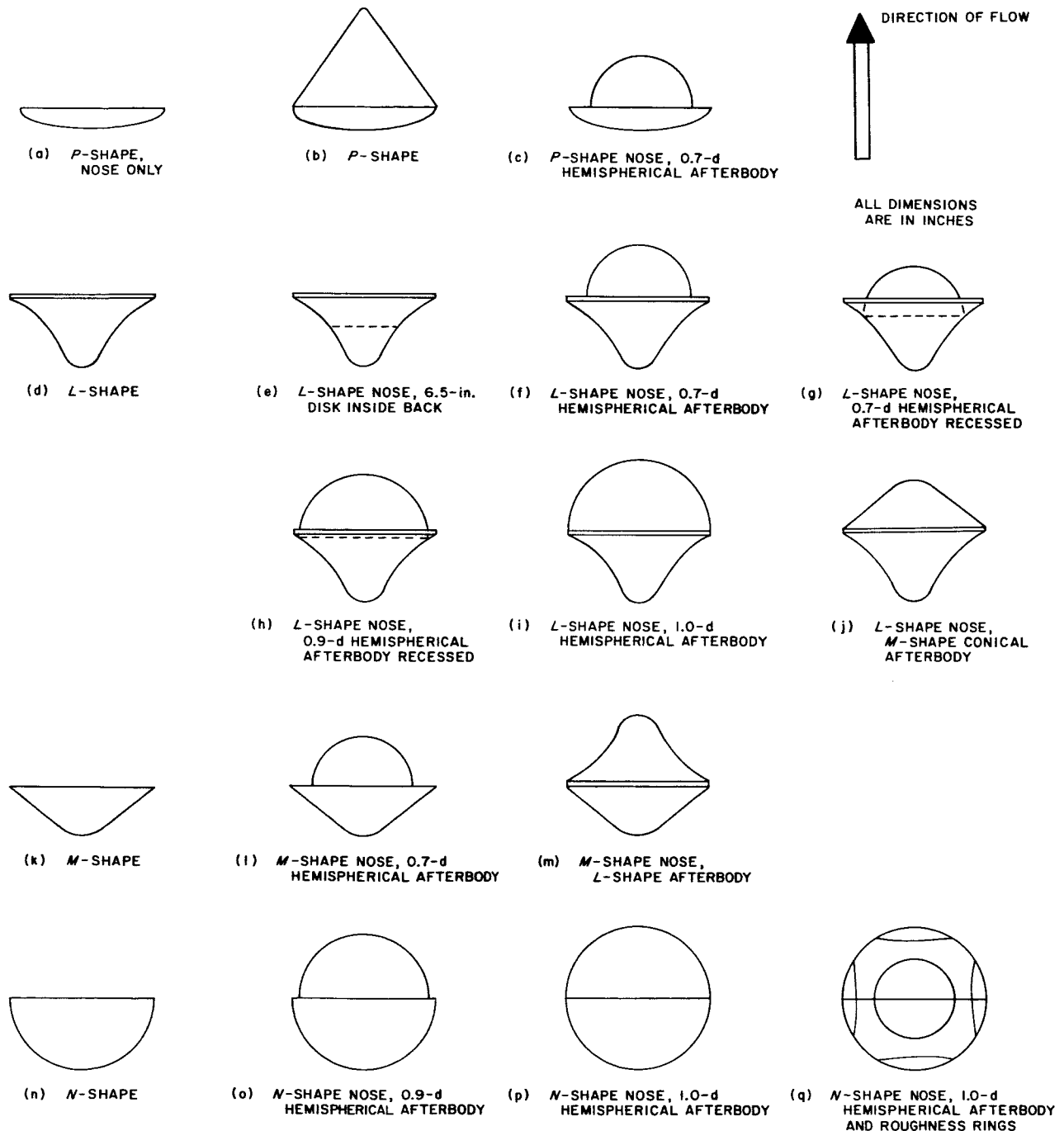


Fig. 11. Sketches of model test configurations

Table 2. Center-of-gravity (c.g.) locations and moments of inertia of the various models tested¹

Configuration	c.g. location ² on the X-axes (in. from nose)	Moments of Inertia (slug-ft ²)	
		X-axes	Y-axes = Z-axes
L	3.02	0.270	0.520
L + cone	3.62	0.292	0.756
L + hemisphere	3.63	0.327	0.947
M	2.64	0.588	0.601
N	2.83	—	0.373
P	2.11	0.648	0.651

¹The values presented in this table are based on an axis system with the origin at the model nose. The values used for the calculations are based on an axis with the origin at the center of mass.

²The Y and Z values of the c.g. were always zero.

launcher released the model when the lights came on. When the desired data had been obtained, the camera was stopped and the model was retrieved.

In order to obtain as much dynamic data as possible, the models were hit with a long pole to supply the impulse for the free oscillation which followed. This method of imparting oscillatory motion to the models resulted in angles of attack as high as 80 deg.

The models were also launched at an angle of attack of 180 deg in order to investigate the orientation characteristics of the different shapes under consideration.

The test runs were made at equilibrium velocities in the range between 49 and 72 ft/sec which resulted in a Reynolds-number range from 0.39 to 0.52×10^6 (based on d).

III. DATA REDUCTION

In addition to qualitative information on the over-all motion of the test configurations, considerable quantitative data were obtained from the motion pictures. These included the drag and pitching-moment coefficients and the dynamic-damping parameter, \bar{C}_{m_q} . Here \bar{C}_{m_q} is defined as the effective constant value of

$$\left\{ \left[\frac{\partial C_m}{\partial \left(\frac{\dot{\alpha} d}{V} \right)} \right] + \left[\frac{\partial C_m}{\partial \left(\frac{\ddot{\alpha} d}{V} \right)} \right] \right\}$$

over a half-cycle of oscillation.

In selecting sections of film for quantitative data reduction, two requirements were made. First, the model must be in approximate equilibrium with the flow; and second, the location in the tunnel must permit accurate measurement of the model's attitude. The requirement for measurement of model angular position further restricted the data reduction to portions of the runs in which the model motion was planar. This was generally the case, but certain configurations occasionally exhibited motion of completely nonplanar character.

Using the axis system as shown in Fig. 12 with its origin at the model c.g., the equations of planar motion in a vertical air stream can be written as:

$$m\ddot{x} = -D + mg \quad (1)$$

$$m\ddot{z} = -Z \quad (2)$$

$$I\ddot{\theta} + M_D\dot{\theta} + M_{\alpha}\alpha = 0 \quad (3)$$

For a model in vertical equilibrium, $m\ddot{x} = 0$. Therefore, Eq. (1) becomes

$$D = mg \quad (4)$$

and in coefficient form

$$C_D = \frac{mg}{1/2\rho AV^2} = \frac{W}{1/2\rho AV^2} \quad (5)$$

In theory, the side force (Z) can be obtained by evaluating the horizontal acceleration from model displacement in the Z-direction as a function of time, and solving Eq. (2) for Z; but the procedure did not prove practical in these tests.

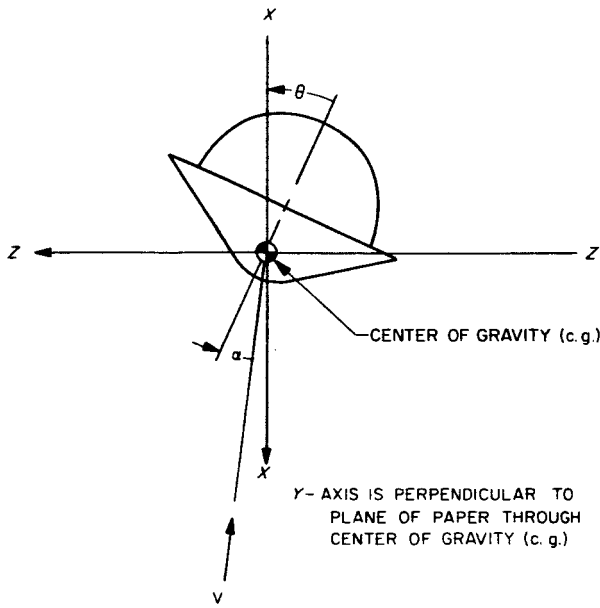


Fig. 12. Axis system

From the solution of Eq. (3) the expression for frequency

$$f = \frac{1}{2\pi} \left(\frac{C_{m_a} A d q}{I} \right)^{1/2} \quad (6)$$

can be obtained for cases where $\left(\frac{M_D}{2I} \right)^2 \ll \left(\frac{M_a}{I} \right)$, as is the case for these tests. This produces the following equation for C_m :

$$C_{m_a} = \left(\frac{32\pi}{d^3 \rho} \right) \frac{I f^2}{V^2} \quad (7)$$

In reducing the wind-tunnel data to the form of a dynamic-damping parameter, extensive use was made of the analysis in Ref. 2. The derivation of that Report was carried out for the vertical-flow case under the assumptions of an axisymmetric model and planar motion.

This led to the following expression for the damping coefficient:

$$\bar{C}_{m_q} = \frac{\left(\frac{m d}{I} \right) \left(\frac{\delta \theta}{\theta_0} \right) \left(\frac{2}{\pi} \right) \left[\frac{C_{m_a}}{(-k_m C_{m_a})^{1/2}} \right] + C_{z_a} - C_x + \frac{g}{k_z V^2}}{\left(\frac{m d^2}{I} \right)} \quad (8)$$

Equation (8) is identical to the expression obtained in Ref. 2 for \bar{C}_{m_q} except for the presence of a gravitational term, viz., the final term in the numerator. For the test conditions, the model was assumed to be in vertical equilibrium with the flow. In this case, $g/k_z V^2 = C_x$ and Eq. (8) reduces to

$$\bar{C}_{m_q} = \frac{\left(\frac{m d}{I} \right) \left(\frac{\delta \theta}{\theta_0} \right) \left(\frac{2}{\pi} \right) \left[\frac{C_{m_a}}{(-k_m C_{m_a})^{1/2}} \right] + C_{z_a}}{\left(\frac{m d^2}{I} \right)} \quad (9)$$

When the C_x and $g/k_z V^2$ terms were evaluated from experimental data, their difference was very small, thus providing a check on the assumption of vertical equilibrium with the flow.

A review of the static data used to obtain the values for C_{m_a} and C_{z_a} in Tables 3 and 4 shows the linear

Table 3. Pitching-moment curve slope (per rad), C_{m_a}

θ (deg)	L*	L + Cone*	L + Hemisphere*	M*	N (Ref. 3)
20	—	—	—	—	-0.721
40	-0.086	-0.063	-0.079	-0.183	-0.550
70	—	—	—	—	-0.096

*Data shown are from JPL Test WT 20-603A. Data from present test were as follows: L (-0.111), L + Cone (-0.151), L + Hemisphere (-0.0728), M (-0.183), and N (-0.364).

Table 4. Side-force curve slope (per rad), C_{z_a}

θ (deg)	L*	L + Cone*	L + Hemisphere*	M**	N (Ref. 3)
20	—	—	—	—	0.620
40	-0.577	-0.719	-0.719	-0.330	0.552
70	—	—	—	—	0.410

*Unpublished data from GALCIT 10-ft wind tunnel, December 1964.
**Data from JPL Test WT 20-603A, September 1964.

Table 6. Other model parameters

Parameters	L	L + Cone	L + Hemisphere	M	N	Units
c.g./d	0.245	0.269	0.269	0.195	0.210	—
W	1547	1312	1772	1779	1193	grams
I_Y	13.60	10.96	13.13	9.52	8.99	(slug-ft ²) $\times 10^3$
$\delta\theta/\theta$	0.072	0.153	0.178	0.202	0.300	—

The angular decay parameter, $(\delta\theta/\theta)$, which is defined as the change in maximum pitch angle at the end of the half-cycle of oscillation, is presented in Table 6 along with the variable physical properties.

In the pitch range at which measurements were made during this test, the angular decay parameter was effectively constant for a given configuration. This aerodynamic parameter, together with C_{m_a} , C_{z_a} and the inertial parameters, when combined in Eq. (9) results in the dynamic-damping parameter, \bar{C}_{m_q} , of Table 7.

Since a more negative value of \bar{C}_{m_q} indicates increased dynamic damping, Table 7 shows the N-shape to be the

Table 7. Dynamic-damping parameter (per rad), \bar{C}_{m_q}

θ (deg)	L	L + Cone	L + Hemisphere	M	N
20	—	—	—	—	-0.319
40	-0.097	-0.132	-0.155	-0.148	-0.281
70	—	—	—	—	-0.204

most highly damped of the configurations tested, followed in order by the M- and L-shapes. The L-shape has a \bar{C}_{m_q} value of about 40% of the N-shape. It should be noted, however, that Table 5 shows the N-shape to possess a $C_D = 0.45$ which is less than half that of the higher drag shapes. This makes it less desirable as an entry configuration. In the case of the N-shape, Table 7 reveals that dynamic damping decreases at higher maximum-pitch angles due to lower values for C_{m_a} and C_{z_a} . This result is expected to hold for the L- and M-shapes for the same reason.

In the case of the L-shape, sufficient data were obtained to show the effect of various afterbodies on the dynamic-damping parameter. For this forebody the addition of a conical or hemispherical afterbody, as illustrated in Fig. 5, substantially increased the dynamic damping. The change resulted mainly from an increase in the $(\delta\theta/\theta)$ term. The afterbodies described above were also tested on the M and N forebody shapes with what appeared to be generally similar results although no quantitative data are available in these cases.

V. DISCUSSION

Considerable qualitative information was gathered from observations made during the tests and from film which was unsuitable for numerical analysis. The motion of any of the shapes changed considerably for the worse when an afterbody, which produced a smooth junction between the fore- and after-body sections of a shape,

was fitted. This combination permitted the flow to remain attached across the junction and resulted in erratic separation from the afterbody which affected the flight path and dynamic stability. A smooth 13.5-in.-d sphere, with c.g./d = 34.7%, moved in a flight path that was erratic to an extent that made more than qualitative

approximation to be good for the *M*-shape and all *L*-shapes for $\theta \leq 40$ deg.

The static coefficients of the *N*-shape were linear only for $\theta \leq 20$ deg (see Ref. 3). The decreasing values of the linear approximation are given at $\theta = 40$ and 70 deg in

the Tables 3 and 4. These values include a weighting factor to account for changing angular velocity with pitch angle, but the numerical values obtained for \bar{C}_{m_q} must be considered less accurate at high θ values. The trend toward lower values of \bar{C}_{m_q} for increasing θ is, however, real for the configurations tested here.

IV. RESULTS

Although a rather small portion of the total test film proved to be of use in obtaining quantitative results, considerable information has been obtained. This section compares data in coefficient form obtained for the *L*, *M* and *N* forebodies described in Section II. Usable film was obtained on the *M* and *N* forebody configurations with flat bases only. In the case of the *L*-shape, data have been obtained from configurations having conical and hemispherical afterbodies, as well as the flat-base case.

In the classified version (JPL TM 33-215, to be published) relating to this Report, the comparison is extended to include an *Apollo*-shape with the c.g. on the axial centerline at 0.156 d aft of the heat shield.

Drag-coefficient data reduced by means of Eq. (5) are presented in Table 5.

Table 5. Dynamic drag coefficient, C_D

θ (deg)	<i>L</i>	<i>L</i> + Cone	<i>L</i> + Hemisphere	<i>M</i>	<i>N</i>
20	1.09	1.10	1.11	—	—
40	—	—	—	0.88	0.45

These data represent an integrated value over the pitch range of the model. The θ column of Table 5 gives a maximum value of pitch to which the model oscillates, rather than a constant angle at which drag data were obtained, i.e., a pitch-envelope value. This value of θ should only be taken as representative of the range since the envelope of θ values changed with time. A 6% reduction in the drag coefficients was applied to account for the lateral-velocity gradient in the tunnel. The models

remained, in general, near the center of the tunnel while the probe, used to measure tunnel velocity, was located near the tunnel wall. The drag coefficients measured during these tests, after the correction, were about 3% higher than values obtained on sting-mounted models at zero pitch angle for comparable velocities and Reynolds number. Values of drag coefficients lower than the zero-pitch values might be expected for these shapes since the drag coefficient decreases with increasing pitch angle. Whether this effect is real and due to the dynamic test situation, lack of sting interference, blockage, and other defects, or is the result of an error in tunnel velocity measurement, is unknown. In any event, the drag coefficient does not enter into the calculation of the dynamic-damping parameter under the assumption of vertical equilibrium.

The pitching moment slope (C_{m_q}) could be obtained directly from the dynamic data of this test by means of Eq. (7). However, static (sting-mounted) data were available for all test configurations and were used in data reduction for the dynamic-damping parameter, in preference to the dynamic data, because of its greater accuracy. The sources of these data are listed in Table 3 along with the data.

The values for C_{z_a} shown in Table 4 were obtained from the same references used for the C_{m_a} values. They are presented here for comparative purposes. The *L*- and *N*-shapes have negative values of C_{z_a} due to the fact that the axial-force component of C_z is predominant over the normal-force component even at small pitch angles. In the case of the *N*-shape, the axial-force component no longer determines the sign of C_{z_a} because the axial force is reduced about 50% while the normal-force coefficient is relatively unchanged.

observations impossible. The configuration appeared to be neutrally stable statically, and slightly unstable dynamically. That this erratic flight path was principally due to wake separation effects was indicated by the improvement resulting from the introduction of large-scale roughness to the sphere surface. This roughness took the form of six rings located on the sphere surface so that each ring was spaced 90 deg from its immediate neighbors. The rings were 7-1/2-in. d and constructed of 3/32-in.-d rod. This roughness reduced considerably the erratic effects due to wake separation and produced what appeared to be slightly-positive static stability along with neutral dynamic stability. When the smooth hemispherical nose was attached to a hemispherical afterbody of

0.70 d, the motion appeared qualitatively similar to the hemisphere-flat back combination; i.e., the flight path was not erratic and pitch oscillations were highly damped. All configurations having hemispherical nose shapes had drag coefficients approximately equal to the *N*-shape.

The configurations under consideration, with the possible exception of the sphere, were dynamically stable following an initial angular displacement of at least 45 deg and in some cases up to 80 deg. Due to the method of testing, this parameter could not be varied systematically. In no case could any of the configurations recover from the tumbling motion induced by launching at $\theta = 180$ deg.

VI. SUMMARY

A summary of the most important conclusions resulting from this study is as follows:

1. The afterbody shape should be chosen to provide a positive point of flow separation behind which reattachment is not possible. Either a rearward-facing step or large angle of expansion near the point of maximum diameter will provide this result.
2. The *L*-shape or *M*-shape forebody configurations combined with a suitable afterbody are the most

suitable shapes for an entry body in the subsonic regime when both \bar{C}_{m_q} and C_D are considered.

3. Any of the successful configurations will stabilize from an initial angular displacement of 45 to 80 deg, but none could recover from the tumbling motion following launch at $\theta = 180$ deg.
4. While the linearized approximations used in reducing the data may cause the numerical values of the dynamic-damping parameter at the higher pitch angles to decrease in accuracy, the general trends indicated in Table 7 are considered to be realistic.

NOMENCLATURE

- A reference area corresponding to maximum body diameter, d
 c.g. center of gravity
 C_D drag coefficient, measured dynamically
 C_m pitching-moment coefficient about Z-axis, M/qAd
 C_{m_α} pitching-moment-coefficient curve slope
 \bar{C}_{m_q} dynamic-damping parameter (constant over a half cycle):

$$\bar{C}_{m_q} = \left\{ \left[\frac{\partial C_m}{\partial \left(\frac{\dot{\theta} d}{V} \right)} \right] + \left[\frac{\partial C_m}{\partial \left(\frac{\dot{\alpha} d}{V} \right)} \right] \right\}$$

- C_X dimensionless aerodynamic force coefficient in X-direction, X/qA
 C_Z dimensionless aerodynamic force coefficient in Z-direction, Z/qA
 C_{Z_α} Z-force-coefficient curve slope
 d reference length, maximum body diameter; also used for the term, diameter, generally
 D drag
 f oscillation frequency, cps
 g gravitational acceleration
 I_Y moment of inertia about the Y-axis
 k_m $\frac{\rho A d}{2I}$
 k_z $\frac{\rho A}{2m}$
 m mass of model
 M_α static pitching-moment curve slope
 M_D pitch-damping moment
 M_r maximum value of a sine-curve pitching moment of index r
 $(\dot{}), (\ddot{})$ first and second derivatives of () with respect to time
 q dynamic pressure, $1/2\rho V^2$
 t time
 V relative velocity of free air stream to model c.g.
 W model weight
 X, Y, Z axes system fixed at model c.g., see Fig. 1
 α angle of attack; the angle between the relative velocity vector and the model centerline, see Fig. 11

NOMENCLATURE (Cont'd)

- γ entry angle (positive is above horizontal)
- $\delta\theta$ angular decay per half cycle
- θ maximum value of angular displacement reached during an oscillation relative to tunnel centerline
- θ_0 initial condition of angular displacement
- ρ free-stream density

REFERENCES

1. *Status of Spin Research for Recent Airplane Designs*, TR-R57, NASA, Washington, D. C., 1960.
2. Jaffe, Peter, *Obtaining Free-Flight Dynamic Damping of an Axially Symmetric Body (At All Angles of Attack) in a Conventional Wind Tunnel*, Technical Report No. 32-544, Jet Propulsion Laboratory, Pasadena, January 15, 1964.
3. von Hansen, M., "Untersuchung einer offenen und geschlossenen Halbkugel (Investigation of an Opened and a Closed Hemisphere)," *Ergebnisse der Aerodynamischen Versuchsanstalt zu Gottingen*, IV Lieferung, 1932.